Topical review: Topological invariants for anomalous Floquet higher-order topological insulators

Biao Huang[1, *]

[1]*Kavli Institute for Theoretical Sciences, University of Chinese Academy of Sciences, Beijing 100190, China*
(Dated: September 26, 2022)

We review the recent development in constructing higher-order topological band insulators under strong periodic drivings. In particular, we focus on various approaches in formulating the anomalous Floquet topological invariants beyond (quasi-)static band topology, and compare their different physical consequences.

CONTENTS

I. INTRODUCTION

Recently, our theoretical tools for quantum many-body systems have been significantly updated by studies on several classes of intrinsically time-dependent problems. For instance, the anomalous Floquet topological insulators for free fermions transcend the traditional characterization by Hamiltonian eigenstates (i.e. static band topology), and requires examinations of evolution operators with genuinely time-dependence [1–3]. Its generalization to interacting cases produces the Floquet symmetry-protected-topological phases [4–10]. Further introducing spatial or internal symmetry breaking into these systems leads to the intriguing Floquet/discrete time crystals [11–13] exhibiting rigid bulk temporal orderings. Among all these phases, a common feature is that one can no longer rely on the thermal equilibrium properties of an effective quasi-static Hamiltonian to understand the physics.

This review focuses one topic for far-from-equilibrium systems, namely, the recent rapid progress of understanding the anomalous Floquet higher-order topological insulators (AFHOTI). We would aim at giving a pedagogical review of the model, features, and constructions of topological indices

unique of these systems. In particular, we would emphasize the subtle differences of topological indices constructed separately in independent works, and point out crucial distinctions of their physical consequences.

AFHOTIs are based on two different fields of anomalous Floquet phases and the higher-order topological insulators. Therefore, it is useful to first review some basic concepts in these two fields and see the need of new concepts and theories for combing them.

For a periodically driven (dubbed Floquet) systems with Hamiltonians $\hat{H}(t + T) = \hat{H}(t)$, one can compare the driving frequency $\omega = 2\pi/T$ with the Hamiltonian internal frequency scales $J/\hbar$, where J denotes the strength of hopping, chemical potential, and etc., to classify problems into different regimes.

Traditionally, one usually handles the following two limits.

1. Higher frequency limit $\omega \gg J/\hbar$, where the internal Hamiltonian system cannot follow the drivings which change rapidly, but instead experiences a time-averaged effect. The lowest order "effective Hamiltonian" here $\hat{H}_{\text{eff}} = \frac{1}{T} \int_0^T dt \hat{H}(t)$ corresponds to the lowest order Magnus expansion in terms of inverse frequencies $1/\omega$. That leads to the so-called Floquet engineering, where one could start from a set of relatively simple and experimentally accessible Hamiltonian $\hat{H}(t)$ at each instant, and end up with a desirable time-independent $\hat{H}_{\text{eff}}$. Examples of Floquet engineering ranges from interactions of solid-state systems with polarized light [14] to the recent cold atom achievement of novel topological phases through Raman or shaken lattice schemes [15–17].

2. Low frequency limit $\omega \ll J/\hbar$ (also dubbed the adiabatic limit), where the external drivings are so slow that the system can approximately relax to and stay in its ground state at each instant. Then, time is just another way to denote certain parameters in the quasi-static Hamiltonian. One well-known example is the Thouless pump for topological insulators, where an adiabatic deformation of the Hamiltonian causes a quantized charge transfer across the whole system [18–20].

In contrast, this review would focus on the third regime where the driving frequency ω is comparable to the Hamiltonian frequency scales $J/\hbar$. That gives rise to a set of so-called "anomalous" Floquet topological phases originally investigated in Refs. [1, 21] concerning the anomalous Floquet Chern insulator. Soon, the anomalous Floquet phases have been generalized to all 10 Altland-Zirnbauer symmetry classes for insulators and also semimetals (see i.e.[2, 3]). The

word "anomalous" refers to a peculiar feature for such systems that all of the Floquet quasienergy bands hosts trivial topology, while robust edge modes still exists due to a new type of time-dependent topology described by the evolution operator. In other words, the time dependence is no longer merely a method of engineering or an adiabatic parameter treated in the static sense, but would play a central role in constructing the anomalous Floquet topology.

Meanwhile, since 2017, a new class of topological phases has emerged dubbed higher-order topological insulators (HOTI) [22–29]. Compared with previous cases where the topological properties of a d-dimensional bulk give rise to $(d-1)$-dimensional boundary states, HOTI features boundary modes of reduced dimensionality. For instance, HOTI in two/three dimensional lattices could host a zero dimensional corner modes, and HOTI in three-dimensions may exhibit a one-dimensional hinge mode along the intersection of two boundary surfaces. For the beginning two years, researchers of HOTI have chiefly been focusing on the static situations [30–38], including extensions to higher order semimetals [39–41], superconductivity [42–48], spin liquids [49] and symmetry-protected-topological phases [50, 51]. Theoretical tools developed therein, such as the static Wannier centers, are based on the eigenstates of Hamiltonians and therefore are intrinsically constrained to static situations. Thus, it is of interest to consider how to introduce the notion of anomalous Floquet phases with time-dependent topology into the realm of HOTIs, and to develop suitable theoretical frameworks to capture their higher-order time-dependent topology.

Breakthroughs on such an issue started from late 2018 [52–55], and have been further developed in the past several years. We would discuss three approaches for computing anomalous Floquet higher-order invariant in this review.

1. **Dynamical polarization theory** [52, 56]. Such an approach generalizes the concept of static higher-order polarization theory into an intrinsically time-dependent situation. Specifically, the static polarization can be characterized by the spatial interference patterns for occupied bands' Bloch waves in different sublattices. In contrast, the dynamical polarization at time $t_0 \in [0, T]$ is formed by the *temporal* interference pattern for Bloch waves at two different instants $t = 0$ and $t = t_0$. In terms of the physical pictures, static polarization characterizes the static centers of collective Wannier functions. Contrarily, the dynamical polarization describes the relative positions of particles evolving from $t = 0$ to $t = t_0$ among different unit cells.

2. **Dynamical singularity methods** [57–59]. This approach generalizes the previous discussion for first-order anomalous Floquet topology into the higher-order setting. Specifically, the evolution operator depends on quasimomenta $\boldsymbol{k}$ and time $t \in [0, T]$. They form a $(d+1)$ dimensional parameter space for a spatially d-dimensional system. For topologically nontrivial systems, their spectrum could exhibit gapless points at certain $(\boldsymbol{k}, t)$, dubbed dynamical singularities, each carrying a nontrivial Berry charge like a Weyl point. The dif-

ference between first and higher-order cases is that the latter situation would involve multiple dynamical singularities which may be prevented to annihilate each other by crystalline and/or onsite symmetries.

3. **Crystalline symmetry graded invariants** [54, 55, 60]. Consider for instance a mirror symmetry M_{xy} mapping quasimomentum $k_x \leftrightarrow k_y$. Then, $M_{xy}(\boldsymbol{k}) = \boldsymbol{k}$ defines an invariant space $k_x = k_y$ with dimensionality reduced by one compared with the dimension of the original Brillouin zone. In such a reduced invariant Brillouin zone, one could then compute certain mirror-graded anomalous Floquet topological invariants to describe the higher-order topology. This approach shares certain similarity with earlier development of (the first order) crystalline topological insulators, see i.e. Ref [61]. In particular, for mirror symmetries, due to the Brillouin zone dimension reductions by 1, the second order topological insulators in $(d+1)$ spatial dimensions exhibit the same classifications as d-dimensional first order topological insulators [55, 60].

The above approaches have been discussed separately in different works. They all capture certain aspects of the anomalous Floquet higher-order topology. However, it is important to note that they are *not* equivalent to each other. Certain systems may show one type of dynamical topology but not the other. One major task of this review is to compare and contrast different approaches in a unified setting in order to highlight their different physical implications — see Sec. V.

Now, we review the Floquet formalism that will be exploited throughout later discussions. The evolution operator $\hat{U}(t)$ for a time-dependent Hamiltonian $\hat{H}(t)$ reads

$$\hat{U}(t) = P_\tau \exp\left((-i/\hbar)\int_0^t d\tau\, \hat{H}(\tau)\right), \qquad (1)$$

where P_τ denotes time-ordering. For a periodically driven (Floquet) system $\hat{H}(t + T) = \hat{H}(t)$, the Floquet operator corresponds to the evolution operator at period ends $\hat{U}_F = \hat{U}(T)$, which is a time-independent operator. The eigenvalues E_α for

$$\hat{U}_F|E_\alpha\rangle = e^{iE_\alpha}|E_\alpha\rangle \qquad (2)$$

denotes the quasi-energy which are defined modulo 2π. Here E_α and the eigenstates $|E_\alpha\rangle$ do not explicitly carry the dependence on time, and could be treated as Floquet quasienergy bands analogous to static Hamiltonian bands. Aside from the $\hat{U}_F$ describing physics at period ends, the evolution operator $\hat{U}(t)$ also contains the information of "micromotions" for evolutions *within* each period. It is then useful to decompose $\hat{U}(t)$ in the following fashion:

$$\hat{U}(t) = \hat{U}_\varepsilon(t)[\hat{U}_F]_\varepsilon^{t/T}. \qquad (3)$$

Here, we take the t/T root for the eigenvalues of the Floquet operator $\hat{U}_F$.

$$[\hat{U}_F]_\varepsilon^{t/T} = \sum_\alpha |E_\alpha\rangle \left(e^{iE_\alpha}\right)_\varepsilon^{t/T} \langle E_\alpha|. \qquad (4)$$

The subscript ε denote the branch cut when taking roots for complex numbers e^{iE_α}. For instance, let $e^{iE_\alpha} = -i$, then $(e^{iE_\alpha})^{t/T}_{\varepsilon=0} = e^{i(3\pi/2)(t/T)}$, while $(e^{iE_\alpha})^{t/T}_{\varepsilon=\pi} = e^{i(-\pi/2)(t/T)}$. At period ends $t = T$ they both converge to the same e^{iE_α}, but different ε would give distinct $[\hat{U}_F]^{t/T}_\varepsilon$ during $t \in (0,T)$. Finally, the micromotions for dynamics within a period is factored into $\hat{U}_\varepsilon(t + T) = \hat{U}_\varepsilon(t)$ after $\hat{U}(t)$ and $[\hat{U}_F]^{t/T}_\varepsilon$ are given. In some sense, this is a time-domain Bloch theorem analogous to the spatial one, where the temporal translation symmetry gives rise to an accumulative part $[\hat{U}_F]^{t/T}_\varepsilon$ and also a periodic part $\hat{U}_\varepsilon(t)$.

In this review, we would chiefly focus on the time-dependent part prescribed by $\hat{U}_\varepsilon(t)$. In comparison, $[U_F]^{t/T}_\varepsilon$ simply gives a linear expansion for quasienergy spectrum in Eq. (4), while the eigenstates $|E_\alpha\rangle$ are time-independent. Therefore, $[U_F]^{t/T}_\varepsilon$ carries the same information as the time-independent Floquet operator $\hat{U}_F$ that can be described by conventional band theories for a static Hamiltonian.

The remaining part of this review is organized as follows. In Sec. II we discuss a model serving as a unified platform to test various topological invariants computed later on. In Sec. III and IV we would introduce two types of approaches characterizing the real-space edge topology (dynamical polarization) and reduced Brillouin zone topology (dynamical singularity and crystalline symmetry graded invariants) respectively. Their differences will be contrasted in Sec. V. Finally we conclude with a discussion of current progresses on this field in Sec. VI.

II. EXEMPLARY MODEL AND ITS FEATURES

For conciseness and also to compare different approaches in a unified setting, we will use the same model in Ref. [52] throughout this review, with a minor extension in Sec. V. The periodically driven Hamiltonian $\hat{H}(t + T) = \hat{H}(t)$ switches between two settings within each period T, where $\hat{H}(t) = \sum_{kmn} \hat{c}^\dagger_{km}|0\rangle [H(\boldsymbol{k},t)]_{mn}\langle 0|\hat{c}_{kn}$, and the matrix $H(\boldsymbol{k},t)$ reads

$$H(\boldsymbol{k},t) = \begin{cases} \gamma' h_1, & t \in [0, T/4]; \\ \lambda' h_{2\boldsymbol{k}}, & t \in (T/4, 3T/4]; \\ \gamma' h_1, & t \in (3T/4, T] \end{cases},$$

$$h_1 = \tau_1\sigma_0 - \tau_2\sigma_2$$

$$h_{2\boldsymbol{k}} = \cos k_x \tau_1\sigma_0 - \sin k_x \tau_2\sigma_3 - \cos k_y \tau_2\sigma_2 - \sin k_y \tau_2\sigma_1.$$

(5)

Throughout this paper, we would use Latin letters m, n to denote sublattices, while Greek letters α, β are reserved for band/branch indices. $\tau_{1,2,3}, \sigma_{1,2,3}$ are Pauli matrices spanning the basis for 4 sublattices $(\hat{c}_{k1}, \hat{c}_{k2}, \hat{c}_{k3}, \hat{c}_{k4})^T$, and τ_0, σ_0 are 2 by 2 identify matrices. Here γ', λ' are hopping constants. The system is controlled by two independent dimensionless numbers $(\gamma, \lambda) \equiv (\gamma' T/2\hbar, \lambda' T/2\hbar)$, and all energy (or time) carry units $2\hbar/T$ (or $T/2$).

Note that the time origin in Eq. (5) is shifted to make it transparent $H(\boldsymbol{k},t) = H(\boldsymbol{k},-t)$. This is chiefly to make it clear that the model satisfies time-reversal as well as chiral symmetries. But one should note that the model is only made of two

driving steps. For certain analysis that does not require a chiral symmetry, such as the dynamical polarization construction in the next section, it is unnecessary to perform such a shift. Here we stick to this artificial three-step formalism so as to compare different approaches consistently.
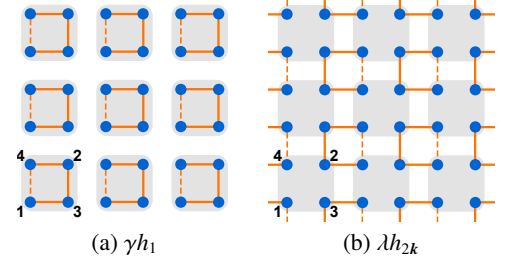

FIG. 1. Figures taken from Ref. [52] for the model in Eq. (5). Solid/Dashed lines denotes $+/-$ sign for the hopping amplitude so each plaquette carries π-fluxes.

To pave the way for later discussions of anomalous Floquet physics, we first focus on the Floquet operator at period ends

$$\hat{U}_F = \sum_{kmn} \hat{c}^\dagger_{km}|0\rangle [U(\boldsymbol{k},T)]_{mn}\langle 0|\hat{c}_{kn} \qquad (6)$$

to understand the features of this model. Under periodic boundary conditions, one can analytically obtain the spectrum as $\pm E_{\boldsymbol{k}}$ with each band doubly degenerate, and $E_{\boldsymbol{k}} = \arccos\left[\cos(\sqrt{2}\gamma)\cos(\sqrt{2}\lambda) - \frac{\cos k_x + \cos k_y}{2}\sin(\sqrt{2}\gamma)\sin(\sqrt{2}\lambda)\right]$. Then, the bulk gap closing condition $E_{\boldsymbol{k}} = 0$ gives the phase boundary

$$\sqrt{2}\lambda = \pm\sqrt{2}\gamma + n\pi, \qquad n \in \mathbb{Z}, \qquad (7)$$

as shown in Fig. 2 (a). Among the four distinct phases we would be interested in the anomalous Floquet phase denoted by ④. Via an exact diagonalization of $\hat{U}_F$ in real space under open boundary conditions, we have the spectrum in Fig. 2 (c) (left pannel). It is clear that there are in-gap corner modes in both quasienergy 0 and π. As the Floquet band topological invariants, such as the band polarization, describe the difference of corner mode numbers above and below certain bands, the identical number of corner modes sandwiching each band indicates a completely trivial static band topology.

To quickly verify it, one can directly take a special parameter point to analytically see the incapability of static band topology to describe anomalous Floquet physics. Let $\sqrt{2}(\gamma, \lambda) = (0.5, 1)\pi$ residing deep inside phase ④, the Floquet operator for Eq. (5) reduces to $U(\boldsymbol{k},T) = ih_1/\sqrt{2}$. We see that here $U(\boldsymbol{k},T)$ and therefore its eigenstates do not even depend on quasimomenta $\boldsymbol{k}$. Since any topological invariants necessarily involves a partial derivative with respect to k_x, k_y, any static topological number must be trivial in such a case. Numerical calculations for more generic parameters are also presented in Fig. 2 (c) and (d). One can also directly compute the band polarization in each phase to verify the vanishing of static band topology for phase ④ [52]. Then, we are forced to go beyond the static descriptions and seek for dynamical characterizations of higher-order anomalous Floquet topology as will be discussed in the following sections.

(a) Phase diagram

(b) One of the corner states

(c) Spectrum for the anomalous Floquet phase.
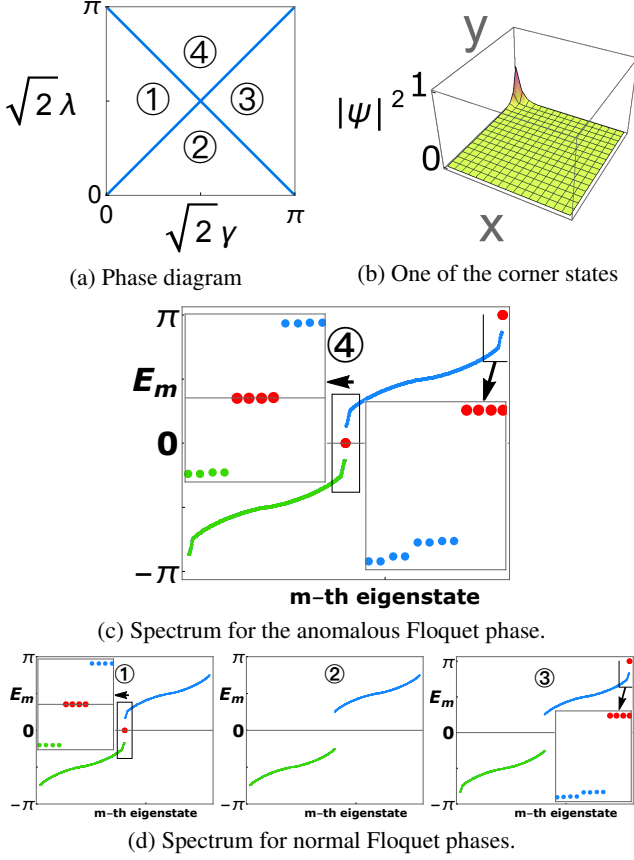
(d) Spectrum for normal Floquet phases.

FIG. 2. Figures taken from Ref. [52]. (a) Phase diagram parameterized by dimensionless $(\gamma, \lambda) \equiv (\gamma'T/2\hbar, \lambda'T/2\hbar)$. (b) One representative in-gap corner state amplitude in phase ④, with others in different corners. (c) – (d) Open-boundary spectrum ($L_x \times L_y = 20 \times 20$) in different phases. Parameters are $\sqrt{2}(\gamma, \lambda) = (\frac{\pi}{4}, \frac{\pi}{2}), (\frac{\pi}{2}, \frac{\pi}{4}), (\frac{3\pi}{4}, \frac{\pi}{2}), (\frac{\pi}{2}, \frac{3\pi}{4})$ for phases ①~④ respectively.

III. TOPOLOGY AT THE BOUNDARY

The dynamical polarization theory describes the co-movement of particles along orthogonal directions, as schematically depicted in Fig. 3. The first order polarization $\pm v_x$ moves along $\pm x$ directions. Based on that, the second order polarization serves as a co-movement along y in addition to the motion of $\pm v_x$. Corner modes then results from obstructing the motions by open boundaries. As such, intuitively it describes the dynamical topology of the real-space boundary for the branches $\pm v_x$. Such a point will be verified further in Sec. V. We also mention that the bulk polarization enforced boundary topology shares similarity with static case of the so-called *boundary obstructed topological phases* [62] described by the static polarization theory.

A. Dynamical polarization theory

In the previous section, we have seen that in the anomalous Floquet phases, all static polarization based on Floquet band
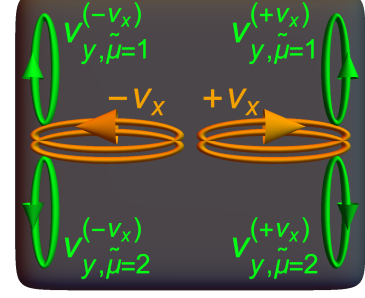

FIG. 3. Figure taken from Ref. [52]. Schematic illustration of dynamical polarization.

wave functions becomes trivial despite the existence of robust corner modes. Now, we review the construction of dynamical polarization for the "anomalous" part $\hat{U}_\varepsilon(t)$ in Eq. (3). As $\hat{U}_\varepsilon(0) = \hat{U}_\varepsilon(T)$ are trivially identity operators, and that $\hat{U}_\varepsilon(t)$ can be gapless at any instants (see examples in the next section for dynamical singularity), it is not meaningful to discuss "band polarization" for such an operator. Instead, one needs to consider the *evolution* for particle polarization throughout a period. The Resta's position operator [63] satisfying periodic boundary condition reads

$$\hat{x} = \sum_{im} \hat{c}_{im}^\dagger |0\rangle e^{-i\frac{2\pi}{L_x}x_i}\langle 0|\hat{c}_{im} = \sum_{k,m} \hat{c}_{k+\frac{2\pi}{L_x}e_x,m}^\dagger |0\rangle\langle 0|\hat{c}_{km}, \quad (8)$$

$$\hat{c}_{im} = \frac{1}{\sqrt{L_x}} \sum_k e^{-i k \cdot r_i} \hat{c}_{km}, \qquad r_i = (x_i, y_i) \quad (9)$$

where L_x means unit cell numbers along x-direction, and the unit cell indices $x_i = 0, 1, \ldots, (L_x - 1)$. Now that we are interested in the evolution of polarization, it may be reasonable to start from

$$\hat{x}(t) = \hat{U}_\varepsilon^\dagger(t)\hat{x}\hat{U}_\varepsilon(t). \quad (10)$$

However, such an operator describing a single moment amounts to simply reshuffling the unit-cell labels, and the eigenvalues of $\hat{x}(t)$ are identical to those for the bare position operator $\hat{x}$ [52]. Instead, a meaningful approach should compare the relative motions between two instants via the following dynamical mean polarization operator

$$\hat{x}_{\text{mean}}(t) = \frac{\hat{x}(0) + \hat{x}(t)}{2}. \quad (11)$$

Here, we would demonstrate what it describes physically through a toy example, and list the practical procedures to compute arbitrarily higher-order dynamical polarization through $\hat{x}_{\text{mean}}(t)$.

An idealized scenario is shown in Fig. 4, where the anomalous evolution takes any site to its neighboring unit cell $x_{i+1} = x_i + 1$ as $\hat{U}_\varepsilon(t_0) = \sum_{im} \hat{c}_{i+1,m}^\dagger |0\rangle\langle 0|\hat{c}_{im}$. If we only check a single
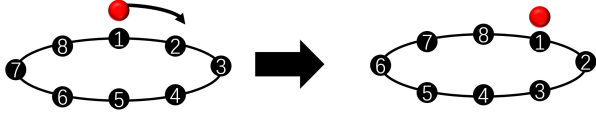
FIG. 4. Toy scenario showing the need for $\hat{x}_{\mathrm{mean}}(t)$.

moment at t_0, we have

$$
\hat{x}(t_0) = \sum_{im} \hat{c}^\dagger_{(i-1),m}|0\rangle e^{-i\frac{2\pi}{L_x}x_i}\langle 0|\hat{c}_{(i-1),m}
$$
$$
= \sum_{im} \hat{c}^\dagger_{i,m}|0\rangle e^{-i\frac{2\pi}{L_x}(x_i+1)}\langle 0|\hat{c}_{i,m} \tag{12}
$$

However, the seeming change from $x_i \to (x_i + 1)$ in the exponential part of Eq. (12) can be canceled by a unit-cell relabeling $i \to i+1$, as shown in Fig. 4. Then, $\hat{x}$ and $\hat{x}(t)$ hosts exactly the same set of eigenvalues $e^{i\frac{2\pi}{L_x}x_i}$, $x_i = 0, 1, \ldots, L_x - 1$, and therefore cannot capture any dynamical information. In contrast, if one adopt $\hat{x}_{\mathrm{mean}}(t)$ in Eq. (11), by combining Eqs. (8) and (12) we have

$$
\hat{x}_{\mathrm{mean}}(t_0) = \sum_{im} \hat{c}^\dagger_{im}|0\rangle \frac{e^{i\frac{2\pi}{L_x}x_i} + e^{i\frac{2\pi}{L_x}(x_i+1)}}{2}\langle 0|\hat{c}_{im} \tag{13}
$$
$$
= \sum_{im} \hat{c}^\dagger_{im}|0\rangle e^{-i\Delta_x(x_i+1/2)}\cos(\pi/L_x)\langle 0|\hat{c}_{im}. \tag{14}
$$

We see that the eigenvalues of $\hat{x}_{\mathrm{mean}}(t)$ exhibits a shift in the exponential part from $x_i \to (x_i + 1/2)$ compared with $\hat{x}$, which cannot be removed by any unit-cell relabeling. Importantly, the shift $\nu = 1/2$ characterize a movement by 2ν from $t = 0$ to $t = t_0$, instead of Wannier function centers as for the static polarization. Finally, it can be proved that the eigenvalues of $\hat{x}_{\mathrm{mean}}(t)$ converges to a unitary phase factor as $O(1/L_x^2)$ when $L_x \to \infty$ for a generic $\hat{U}_\varepsilon(t)$ [52].

Next, we outline the procedure to apply $\hat{x}_{\mathrm{mean}}(t)$ to obtain dynamical higher-order polarization in the thermodynamic limit $L_x, L_y \to \infty$.

1. The first order polarization can be obtained by computing the dynamical Wilson loop $W_{x,\boldsymbol{k}}(t)$:

$$
\hat{x}^{L_x}_{\mathrm{mean}}(t) = \sum_{\boldsymbol{k}mn} \hat{c}^\dagger_{\boldsymbol{k}m}|0\rangle [W_{x,\boldsymbol{k}}(t)]_{mn}\langle 0|\hat{c}_{\boldsymbol{k}n}
$$
$$
W_{x,\boldsymbol{k}}(t) = P_{k'_x}e^{-\frac{1}{2}\int_{\boldsymbol{k}}^{\boldsymbol{k}+2\pi\boldsymbol{e}_x}dk'_x U^\dagger_\varepsilon(\boldsymbol{k}',t)\partial_{k'_x}U_\varepsilon(\boldsymbol{k}',t)}, \tag{15}
$$

Then, the first order dynamical branches μ characterizing movement of particles along x can be obtained by diagonalizing the dynamical Wilson loop,

$$
\sum_n [W_{x,\boldsymbol{k}}(t)]_{mn}[\nu_{x,\mu}(\boldsymbol{k},t)]_n = e^{-2\pi i\nu_{x,\mu}(k_{l\neq x},t)}[\nu_{x,\mu}(\boldsymbol{k},t)]_m, \tag{16}
$$
$$
|b_{x,\mu}(x_i, k_{l\neq x}, t)\rangle = \frac{1}{\sqrt{L_x}}\sum_{k_x,m}\hat{c}^\dagger_{\boldsymbol{k}m}|0\rangle e^{ik_x x_i}[\nu_{x,\mu}(\boldsymbol{k},t)]_m. \tag{17}
$$

One can verify that

$$
\hat{x}_{\mathrm{mean}}(t)|b_{x,\mu}(x_i, k_{l\neq x}, t)\rangle = e^{-i\frac{2\pi}{L_x}(x_i+\nu_{x,\mu}(k_{l\neq x},t))}|b_{x,\mu}(x_i, k_{l\neq x}, t)\rangle, \tag{18}
$$

where $\nu_{x,\mu}(k_{l\neq x},t)$ characterizes the movement of particles from time 0 to t by $2\nu_{x,\mu}(k_{l\neq x},t)$ along x, away from the unit-cell positions x_i.

2. The second order polarization along the orthogonal direction y can be constructed by first projecting the $\hat{y}_{\mathrm{mean}}(t) =$ onto the first order branches. To do so, we group the first order branches μ's into several separable sets ν_x. Two branches μ_1, μ_2 in different sets should be completely separable $\nu_{x,\mu_1}(k_{l\neq x}t) \neq \nu_{x,\mu_2}(k_{l\neq x},t)$ for all $k_{l\neq x}, t$. Then,

$$
\hat{y}^{(\nu_x)}_{\mathrm{mean}}(t) = \hat{P}_{\nu_x}\frac{\hat{y}(t) + \hat{y}(0)}{2}\hat{P}_{\nu_x}, \tag{19}
$$
$$
\hat{P}_{\nu_x} = \sum_{x_i,k_{l\neq x};\mu\in\nu_x}|b_{x,\mu}(x_i, k_{l\neq x}, t)\rangle\langle b_{x,\mu}(x_i, k_{l\neq x}, t)| \tag{20}
$$

Then, one can perform the same procedure as the first order dynamical polarization,

$$
\left(\hat{y}^{(\nu_x)}_{\mathrm{mean}}(t)\right)^{L_y} = \sum_{\boldsymbol{k},\mu_1\mu_2\in\nu_x}\hat{b}^\dagger_{\boldsymbol{k}\mu_1}(t)|0\rangle[W^{(\nu_x)}_{y,\boldsymbol{k}}]_{\mu_1\mu_2}\langle 0|\hat{b}_{\boldsymbol{k}\mu_2} \tag{21}
$$
$$
\hat{b}^\dagger_{\boldsymbol{k}\mu}(t) = \sum_m \hat{c}^\dagger_{\boldsymbol{k}m}[\nu_{x,\mu}(\boldsymbol{k},t)]_m, \tag{22}
$$
$$
\sum_{\mu_2}[W^{(\nu_x)}_{y,\boldsymbol{k}}(t)]_{\mu_1\mu_2}[\nu_{y,\tilde{\mu}}(\boldsymbol{k})]_{\mu_2} = e^{2\pi i\nu^{(\nu_x)}_{y,\tilde{\mu}}(k_{l\neq y},t)}[\nu^{(\nu_x)}_{y,\tilde{\mu}}(\boldsymbol{k},t)]_{\mu_1}, \tag{23}
$$

and obtain the second order dynamical branches $\tilde{\mu}$'s. If we limit our discussions to the second order polarization, the quadrupolar motions are then

$$
\langle\nu^{(\nu_x)}_{y,\tilde{\mu}}\rangle(t) = \int_{-\pi}^{\pi}\frac{dk_x}{2\pi}\nu^{(\nu_x)}_{y,\tilde{\mu}}(k_x, t). \tag{24}
$$

3. For even higher order polarization, such a procedure can be directly generalized. For instance, a third order polarization would involve projecting $\hat{z}_{\mathrm{mean}}(t)$ onto a set of second-order dynamical branches similar to Eqs. (17), (19) and (20). Its associated dynamical Wilson loop with give rise to the third order branches, so on and so forth. One can check Ref. [56] for the example of calculating the third order dynamical polarization for an eight-band higher-order topological superconductor.

B. Numerical results

In practical calculations, usually the analytical form of $\hat{U}_\varepsilon(t)$ cannot be easily accessed, and one has to perform numerical calculations for a finite-size lattice of size $L_x \times L_y \times L_z \times \ldots$. Here, we give the corresponding formulae for such a finite size sample for reference. The starting point is the matrix $U_\varepsilon(\boldsymbol{k}, t)$ for the anomalous part of evolution operators $\hat{U}_\varepsilon(t) = \sum_{\boldsymbol{k}mn}\hat{c}^\dagger_{\boldsymbol{k}m}|0\rangle[U_\varepsilon(\boldsymbol{k}, t)]_{mn}\langle 0|\hat{c}_{\boldsymbol{k}n}$. The Brillouin zone is discretized into steps of $\Delta_{x,y} = 2\pi/L_{x,y}$ along k_x or k_y Then,

1. The first order dynamical Wilson loop

$$
Q_{x,\boldsymbol{k}}(t) = \frac{\mathbb{I} + U^\dagger_\varepsilon(\boldsymbol{k} + \Delta_x\boldsymbol{e}_x, t)U^\dagger_\varepsilon(\boldsymbol{k}, t)}{2}, \tag{25}
$$
$$
W_{x,\boldsymbol{k}}(t) = Q_{x,\boldsymbol{k}+(L_x-1)\Delta_x\boldsymbol{e}_x}(t)\ldots Q_{x,\boldsymbol{k}+\Delta_x\boldsymbol{e}_x}(t)Q_{x,\boldsymbol{k}}(t) \tag{26}
$$

Its eigenvalues and eigenstates are obtained as

$$\sum_n [W_{x,\boldsymbol{k}}(t)]_{mn}[\nu_{x,\mu}(\boldsymbol{k},t)]_n = e^{2\pi i \nu_{x,\mu}(k_{l\neq x},t)}[\nu_{x,\mu}(\boldsymbol{k},t)]_m \quad (27)$$

Note that the matrix $W_{x,\boldsymbol{k}}(t)$ has the *same* dimension as the number of sublattices.

2. The second order results are

$$[Q^{(\nu_x)}_{y,\boldsymbol{k}}(t)]_{\mu_1\mu_2} = \sum_{m_1 m_2} [\nu_{x,\mu_1}(\boldsymbol{k}+\Delta_y\boldsymbol{e}_y,t)]^*_{m_1}$$

$$\times \left[\frac{\mathbb{I} + U^\dagger_\varepsilon(\boldsymbol{k}+\Delta_y\boldsymbol{e}_y,t)U_\varepsilon(\boldsymbol{k},t)}{2}\right]_{m_1 m_2} [\nu_{x,\mu_2}(\boldsymbol{k},t)]_{m_2}, \quad (28)$$

$$W^{(\nu_x)}_{y,\boldsymbol{k}}(t) = Q^{(\nu_x)}_{y,\boldsymbol{k}+(L_y-1)\Delta_y\boldsymbol{e}_y}(t) \cdots Q^{(\nu_x)}_{y,\boldsymbol{k}+\Delta_y\boldsymbol{e}_y}(t)\, Q^{(\nu_x)}_{y,\boldsymbol{k}}(t) \quad (29)$$

Here, $\mu_1,\mu_2 \in \nu_x$ belongs to the same set of first order branches whose $\nu_{x,\mu_1}(k_{l\neq x},t) = \nu_{x,\mu_2}(k_{l\neq x},t)$ intersect at certain $k_{l\neq x},t$. Therefore, the dimension of $W^{(\nu_x)}_{y,\boldsymbol{k}}(t)$ is generally smaller than the number of sublattice. Similar to the first order case, we diagonalize the dynamical Wilson loop at each instant

$$\sum_{\mu_2} [W^{(\nu_x)}_{y,\boldsymbol{k}}]_{\mu_1\mu_2}[\nu^{(\nu_x)}_{y,\tilde\mu}(\boldsymbol{k},t)]_{\mu_2} = e^{2\pi i \nu^{(\nu_x)}_{y,\tilde\mu}(k_{l\neq x},t)}[\nu^{(\nu_x)}_{y,\tilde\mu}(\boldsymbol{k},t)]_{\mu_1}. \quad (30)$$

3. If even higher-order polarization is needed, we simply repeat the calculation in Eqs. (28) – (30) for polarization along additional orthogonal directions until one can no longer separate the branches into completely separable sets. Here for conciseness we would stop at the second order. Then, the last step is to compute the averaged dynamical polarization

$$\langle \nu^{(\nu_x)}_{y,\tilde\mu}\rangle(t) = \frac{1}{L_y}\sum_{k_{l\neq x}} \nu^{(\nu_x)}_{y,\tilde\mu}(k_{l\neq x},t) \quad (31)$$

Now, we test the above algorithm against the model shown in Fig. 1. Due to the two mirror symmetries

$$M_x U_\varepsilon(k_x,k_y,t)M_x^{-1} = U_\varepsilon(-k_x,k_y,t),$$
$$M_y U_\varepsilon(k_x,k_y,t)M_y^{-1} = U_\varepsilon(k_x,-k_y,t), \quad (32)$$
$$M_x = \tau_1\sigma_3, \qquad M_y = \tau_1\sigma_1, \quad (33)$$

the structure of various dynamical branches are constrained. There are four sublattice in the system, and therefore we have 4 first order dynamical branches $\nu_{x,\mu}(k_y,t)$, $\mu = 1,2,3,4$ as in Eq. (27) with respect to each ε lying in a certain gap ($\varepsilon = 0$ or $\varepsilon = \pi$). These branches separate into two sets $\pm\nu_x$. Each set contains two degenerate branches, giving rise to two second order dynamical polarization branches. Take the set $+\nu_x$ for instance, the second order averaged dynamical polarization is shown in Fig. 5 (b) for the four phases in Fig. 2 (a). For the gap with corner modes, we have the associated $\langle\nu^{(+\nu_x)}_{y,\tilde\mu}\rangle(t)$ going from 0 to 1 (or vice versa) from $t = 0$ to $t = T$. The two branches cross at 0.5, signaling that all particles move to their nearby unit cell along y near the edge of $x_i = L_x - 1$. Then, the
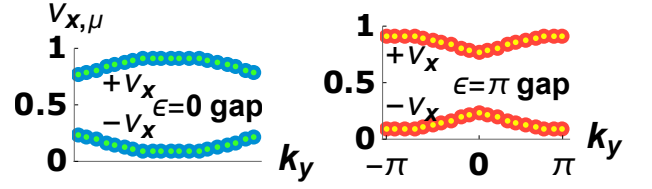
(a) First order dynamical branches at $t = T/2$.
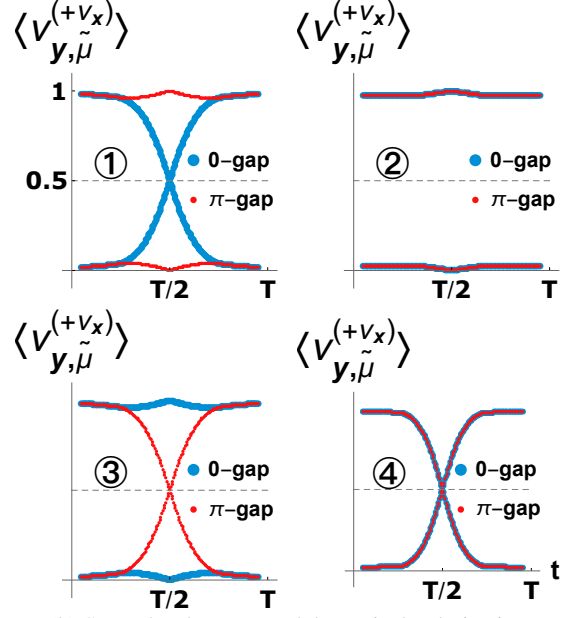
(b) Second order averaged dynamical polarization

FIG. 5. Figures taken from Ref. [52]. (a) Exemplary first-order dynamical branches $\nu_{x,\mu}(k_y,t)$ in phase ④ at $t = T/2$. Four branches for *each* ε-gap separate into two doubly degenerate sets $\pm\nu_x$. Other phases/instants t exhibit $\nu_{x,\mu}(k_y,t)$ of similar structures. (b)–(e) Quadrupolar motions $\langle\nu^{(\nu_x)}_{y,\tilde\mu}\rangle(t)$ in a cycle, with the same parameters as in Fig. 2 for each phase respectively. Generically the $1/2$ crossing needs not to occur at $t = T/2$ if the chiral symmetry is broken.

open boundary serves as an obstruction for motion and lead to a localized corner mode near $x_i = L_x - 1, y_i = 0, L_y - 1$. Similarly physics happens for the $-\nu_x$ first order branches giving rise to another two corner modes around $x_i = 0$. Comparing Fig. 5 (b) with Fig. 2 (c) (d), we see a one-to-one correspondence between non-trivial dynamical polarization in each gap and the existence of corner states therein.

IV. TOPOLOGY OF THE REDUCED BRILLOUIN ZONE

In this section, we review two alternative ways to characterize the anomalous Floquet higher-order topology. They both describe the stable topological properties of certain special regions in the Brillouin zone, typically one or more dimensional lower than the original Brillouin zone.

A. Dynamical singularity (DS)

As mentioned in the introduction, dynamical singularity refers to the gapless points for the spectrum of periodized evolution operator $U_\varepsilon(\boldsymbol{k}, t)$ over the extended parameter space $(\boldsymbol{k}, t)$. For instance, in two spatial dimensions, the 3-dimensional parameter space (k_x, k_y, t) could support various types of Weyl or Dirac points. Specifically, one could obtain the instantaneous spectrum

$$U_\varepsilon(\boldsymbol{k}, t)|u_n(\boldsymbol{k}, t)\rangle = e^{iu_n(\boldsymbol{k}, t)}|u_n(\boldsymbol{k}, t)\rangle. \tag{34}$$

Note that $u_n(\boldsymbol{k}, t)$ is *not* the Floquet spectrum for $U(\boldsymbol{k}, T)|E_{n,\boldsymbol{k}}\rangle = e^{iE_{n,\boldsymbol{k}}}|E_{n,\boldsymbol{k}}\rangle$ but just a theoretical tool to analyze topology. Suppose $E_{n,\boldsymbol{k}}$ exhibits two gaps at 0 and π. Then, the gapless point $(\boldsymbol{k}_0, t_0)$ for instant phase band to touch each other $u_{n_1}(\boldsymbol{k}_0, t_0) = u_{n_2}(\boldsymbol{k}_0, t_0) = 0$ and/or π is called a dynamical singularity. One could further compute its charge through Berry fluxes, similar to the Weyl semimetal cases. To do so, consider a closed parameter surface $S \in \{\boldsymbol{k} \in$ 1st Brillouin zone, $t \in (0, T)\}$ enclosing $(\boldsymbol{k}_0, t_0)$, and the associated Chern number designates the singularity charge

$$Q = C = \int_\Sigma \frac{d\boldsymbol{S}}{2\pi i} \cdot (\boldsymbol{\nabla} \times \langle u_n(\boldsymbol{k}, t)|\boldsymbol{\nabla}|u_n(\boldsymbol{k}, t)\rangle) \tag{35}$$

Multiple Weyl points with opposite charges may merge into the same point $(\boldsymbol{k}_0, t_0)$ and form a charge-neutral Dirac point. Both Weyl and Dirac points mentioned above are all dubbed the dynamical singularities.

Compared with the first order anomalous Floquet insulators, the presence of crystalline symmetries in FHOTI typically will result in multiple DS's related by symmetry. It is then the subject of this section to analyze the stability of DS in such scenario, and to apply this method to the model in Fig. 1 for illustrations.

Consider a certain crystalline symmetry denoted by A, such as rotations or mirror reflections. Generically, under the operation of A, a crystalline momentum will be mapped to a different one $A(\boldsymbol{k}) = \boldsymbol{k}'$. Then, one could define the **reduced Brillouin zone** by the condition $\{\boldsymbol{k}|A(\boldsymbol{k}) = \boldsymbol{k}\}$, which is typically the rotation axis or the mirror reflection plane in the full Brillouin zone.

So far, there have been two approaches depending on whether the DS locate inside the reduced Brillouin zone

(1) DS away from reduced Brillouin zone

In this case, the only effect of a certain crystalline symmetry A is to allocate the relative positions of DS's. For instance, if a DS exists at $(\boldsymbol{k}_0, t_0)$, the others would be fixed at $(A(\boldsymbol{k}_0), t_0), (A^2(\boldsymbol{k}_0), t_0)$ etc. The stability of these DS's would rely on a mechanism similar to the Weyl physics: as long as translation symmetry is preserved (no mixing of different momenta $\boldsymbol{k}$), the DS cannot be gapped out until the perturbation is strong enough to merge two DS's of opposite charges. A natural requirement is then that the DS's are Weyl points rather than Dirac points, as the latter can be generically gapped out by themselves. Consequently, the system should not preserved both time-reversal symmetry and inversion symmetry,

for otherwise the Berry curvature vanishes [64] implying that only Dirac points but not Weyl points could exist. An example exploiting mirror symmetries is shown in Ref. [57]. There, the locations of DS's exhibit a quadruplet pattern at $(\pm k_x, \pm k_y)$ on certain planes of fixed t_0. The topological invariant is then defined as the total Weyl charge within, i.e. the first quadrant of the first Brillouin zone.

It is helpful to stress in what sense does it mean by topology here. Note that the Weyl physics for $U_\varepsilon(\boldsymbol{k}, t)$ applied here only serves as a theoretical tool — the spectrum of Floquet operators $U(\boldsymbol{k}, T)$ is fully gapped. In other words, physically we are investigating an insulator, not a semimetal. Typically one would define a stable topology for insulators if the topological number remains unchanged as long as

1. The bulk gap of $U(\boldsymbol{k}, T)$ remains open;

2. The system preserves the original symmetry when smoothly deformed.

Generically, according to the Weyl physics picture, one could smoothly deform $U_\varepsilon(\boldsymbol{k}, t)$ such that all Weyl points converge to the same point within reduced Brillouin zone at a certain $t \in (0, T)$; such an operation does not violate the underlying symmetry, and does not require a bulk gap closure for $U(\boldsymbol{k}, T)$. Since multiple Weyl points come to the same point and form a degenerate Dirac point, they could surely be gapped out. That means one could smoothly deform the system to gap out the DS's without closing bulk gaps for $U(\boldsymbol{k}, T)$. Therefore, topological numbers defined in this way does not correspond to those in insulators. Rather, it should be understood in terms of microscopic models similar to the case of Weyl semimetals: suppose we have a specific model with a given set of parameters that give rise to DS's with a nontrivial invariant. Then, it is robust against parametrically small perturbations which does not merge Weyl points for the spectrum of $U_\varepsilon(\boldsymbol{k}, t)$.

(2) DS within reduced Brillouin zone

Based on the above discussion, it is also worth exploring whether additional protections can be provided such that DS's cannot be gapped out even if they are merged to the same point in the Brillouin zone. Such a possibility is recently explored in a series of works in two spatial dimensions for chiral [58] and particle-hole [59] symmetric systems. The idea is to endow DS (of either Weyl or Dirac type) additional quantum numbers so that DS's with different conserved quantum numbers are forbidden to hybridize with and gap out each other. To make our discussions concise and also connected with the next subsection, we would focus on the simpler case of mirror crystalline symmetry. Classifications by rotation and dihedral symmetries can be found in Ref. [58, 59].

We use two symmetries to illustrate the physics here. First, consider a mirror symmetry with mirror reflection plane along the diagonal direction, i.e. connecting sublattices 1 and 3 in Fig. 1. That corresponds to the operator

$$M_{xy} = \begin{pmatrix} \sigma_3, & 0 \\ 0 & \sigma_1 \end{pmatrix}, \quad M_{xy}U_\varepsilon(k_x, k_y, t)M_{xy}^{-1} = U_\varepsilon(k_y, k_x, t). \tag{36}$$

Further, we require the system to host chiral symmetry, and focus on the π-gap in the following [3],

$$S = \tau_3\sigma_0, \quad S U_{\varepsilon=\pi}(\boldsymbol{k},t)S^{-1} = U_{\varepsilon=\pi}(\boldsymbol{k},T-t)e^{4\pi i t/T}. \quad (37)$$

The relation $M_{xy}S M_{xy}^{-1} = +S$ means such a set of symmetry hosts $\mathbb{Z}$ classification for each gap of $U(\boldsymbol{k},T)$ [2, 32]. (Note that the classification in [55] is referring to time-glide, not just a mirror symmetry, and therefore different from our current discussions).

Now, since we are interested in the stability of different DS's when they are merged together, it is enough to consider the high symmetry points, namely, the mirror plane $k_x = k_y \equiv k$ and the half-period point $t = T/2$. Denote $\tilde{U}(k) \equiv U_{\varepsilon=\pi}(k_x = k_y = k, T/2)$, the two symmetries are then reduced to commutation relations

$$[M_{xy}, \tilde{U}(k)] = 0, \quad [S, \tilde{U}(k)] = 0. \quad (38)$$

That means we can simultaneously denote the eigenstates with quantum numbers

$$\tilde{U}(k)|m_{xy}, s, \tilde{u}_n(k)\rangle = e^{i\tilde{u}_n(k)}|m_{xy}, s, \tilde{u}_n(k)\rangle,$$
$$M_{xy}|m_{xy}, s, \tilde{u}_n(k)\rangle = m_{xy}|m_{xy}, s, \tilde{u}_n(k)\rangle,$$
$$S|m_{xy}, s, \tilde{u}_n(k)\rangle = s|m_{xy}, s, \tilde{u}_n(k)\rangle \quad (39)$$

where $s = \pm 1, m_{xy} = \pm 1$. Since $\tilde{U}(k)$ in Fig. 1 is a four-dimensional matrix, the two quantum numbers (s, m_{xy}) completely diagonalize the phase band space at each k. Therefore, in the basis of Eq. (39) a Weyl point can be expanded into a diagonal form, i.e.

$$\tilde{U}(k) = e^{i\pi}\left(\mathbb{I} + i\begin{pmatrix} \alpha p & 0 & 0 & 0 \\ 0 & -\alpha p & 0 & 0 \\ 0 & 0 & \beta p' & 0 \\ 0 & 0 & 0 & -\beta p' \end{pmatrix}\right) + O(p^2, (p')^2) \quad (40)$$
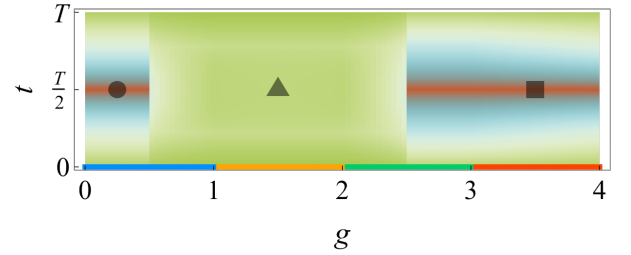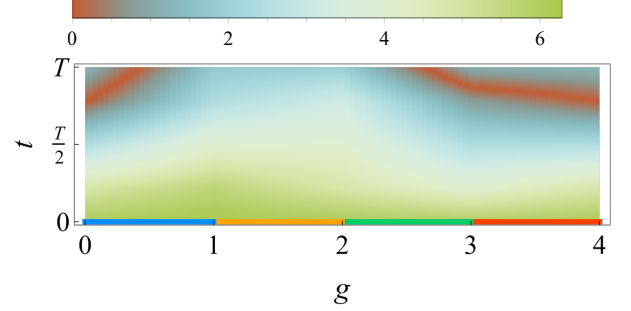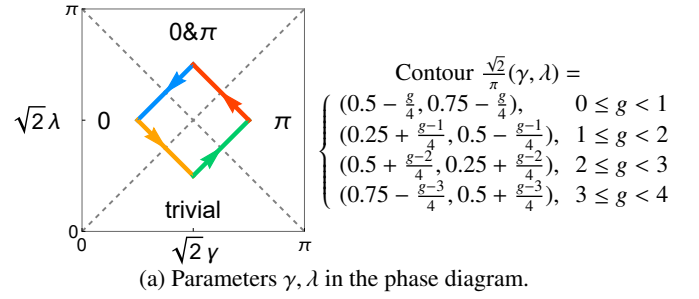
where $p = (k - k_0)$ $(p' = k - k_0')$ and DS's locate at k_0, k_0'. Parameters α, β depend on microscopic details. The four diagonal elements reside on orthogonal subspace labeled by different s, m_{xy}, and therefore there is no off-diagonal elements allowed to hybridize and gap out them.

To verify, we start from the original basis in Eq. (5) and take for instance $\sqrt{2}(\gamma, \lambda) = \pi(0.5, 1)$ where corner states show up in both gaps. Then, a straightforward calculation gives

$$\tilde{U}(k) = -\cos(k)\tau_0\sigma_0 + i\sin(k)\begin{pmatrix} -\sigma_3 & 0 \\ 0 & \sigma_1 \end{pmatrix}, \quad (41)$$

which has the same set of eigen-structure as M_{xy} in Eq. (36). The DS's of π-gap here feature a four-fold degenerate Dirac point at $k = 0$, and it is straightforward to expand $\tilde{U}(k)$ to linear order in the eigen-basis of M_{xy} into the form of Eq. (40) with $\alpha = \beta = 1$. Note also that the upper-left (or lower-right) block corresponds to $s = \pm 1$ for chiral symmetry.

Finally, we give a numerical result for more generic parameters across the phase diagram in Fig. 2 (a), which we reproduce in Fig. 6 (a). To loop over all the four phases, we consider a parameter contour as explained in Fig. 6 (a) parameterized by $g \in [0, 4]$, where $g = 0.5, 1.5, 2.5, 3.5$ are points

(a) Parameters γ, λ in the phase diagram.

Contour $\frac{\sqrt{2}}{\pi}(\gamma, \lambda) =$
$$\begin{cases} (0.5 - \frac{g}{4}, 0.75 - \frac{g}{4}), & 0 \le g < 1 \\ (0.25 + \frac{g-1}{4}, 0.5 - \frac{g-1}{4}), & 1 \le g < 2 \\ (0.5 + \frac{g-2}{4}, 0.25 + \frac{g-2}{4}), & 2 \le g < 3 \\ (0.75 - \frac{g-3}{4}, 0.5 + \frac{g-3}{4}), & 3 \le g < 4 \end{cases}$$

(b) Size of π-gap for the full evolution operator $U(\boldsymbol{k}, t)$

(c) Size of π-gap for the periodized evolution operator $U_{\varepsilon=\pi}(\boldsymbol{k}, t)$. The discontinuity is due to the loss of definition for the branch cut ε of $[U(\boldsymbol{k}, T)]_{\varepsilon=\pi}^{(t/T)}$ (Eq. (4)) when the π-gap closes. Spectrum for three parameter points (denoted by ●, ▲ and ■ is presented in Fig. 7)

FIG. 6. Dynamical singularity when the parameters γ, λ in the model of Fig. 1 takes various values in the phase diagram. (a) Parametrization for different values of γ, λ, where the contour across all 4 phases is parametrized by g. (b) The size of π-gap for $U(\boldsymbol{k}, t)$, where we see that the phase transition is associated with destroying or creating a dynamical singularity at $t = T$. (c) The size of π-gap for the periodized $U_{\varepsilon=\pi}(\boldsymbol{k}, t)$. Due to chiral symmetry for $U_{\varepsilon=\pi}$, the dynamical singularity always occur at $t = T/2$. In (b) and (c), the red-color (for vanishing π-gap) marks the instants where dynamical singularities exist. (d) Representative spectrum at $t = T/2$ for three g values.

at the phase transitions. To illustrate possible dynamical singularities, we compute the π-gap size for the full evolution operator $U(\boldsymbol{k}, t)$ (Fig. 6 (b)) and the periodized evolution operator $U_{\varepsilon=\pi}(\boldsymbol{k}, t)$ (Fig. 6 (c)). At each instant t, the gap size is the smallest value $\Delta_\pi = \min(\{E_1(\boldsymbol{k}, t) - E_2(\boldsymbol{k}, t)|\forall \boldsymbol{k}\})$ between the two sets of bands $E_1, E_2 \in [0, 2\pi]$ over the whole Brillouin zone. Then, $\Delta_\pi = 0$ denotes dynamical singularity for the π-gap.

From Fig. 6 (b), we confirm that dynamical singularities exist for $g < 0.5$ and $g > 2.5$, corresponding to phases ④ and ③ in Fig. 2 (a) as expected. Note that the stable $\Delta_\pi = 0$ here

can only be created or annihilated by moving them towards the period ends $t = T$, namely, by a bulk gap closure for the Floquet operator $U(\boldsymbol{k}, T)$. It is worth noting that the Floquet bulk gap closure and reopening through a continuous change of parameter was exploited to detect dynamical singularities in a recent cold atom experiment [65, 66].

Similarly, we see in Fig. 6 (c) that dynamical singularities show up within the same parameter range for the periodized $U_{\varepsilon=\pi}(\boldsymbol{k}, t)$. Due to the rescaling with $[U(\boldsymbol{k}, T)]_{\varepsilon=\pi}^{-t/T}$ (see Eq. (3)), dynamical singularities all locate at $t = T/2$ for such a chiral-symmetric system. Also, because $U(k, T)$ becomes gapless (for the π-gap) at the phase transitions, the branch cut $\varepsilon = \pi$ becomes ill-defined right at the phase transition point, and therefore a sharp discontinuity is observed in Fig. 6 at $g = 0.5, 1.5$. For concreteness, for the three representative parameter points denoted as ●, ▲ and ■ in Fig. 6 (c), we also plot the instantaneous phase band dispersions in Fig. 7, where the band touching point at $\boldsymbol{k} = \boldsymbol{0}$ is clearly seen in (a) and (c). In all cases, the dynamical singularity here is a four-fold degenerate Dirac point.

B. Crystalline symmetry graded invariants

From the previous discussions, we see that a stable dynamical singularity protected by the bulk gap of Floquet operators $U(\boldsymbol{k}, T)$ would require examinations of the reduced Brillouin zone defined by i.e. $M_{xy}(\boldsymbol{k}) = \boldsymbol{k}$. Such an operation reduces the dimension of k-space by 1. If we constrain ourselves to the second-order topological insulator/superconductors, there is a straightforward way to capture the second-order indices by applying a first-order-like (mirror-graded) index in the reduced Brillouin zone. This approach actually originates from the earlier studies of (static) topological crystalline insulators [61]. It has been applied in a number of scenarios including static and anomalous Floquet insulators of higher-orders [32, 55, 60, 67, 68].

Let us illustrate the method through the model in Fig. 1 using still the two symmetries, M_{xy}, S, as in Eqs. (36) and (37). For a chiral symmetric system, at $t = T/2$, the anomalous evolution operator takes diagonal/off-diagonal form depending on which gap we check [2, 3],

$$U_{\varepsilon=0}(k, \frac{T}{2}) = \begin{pmatrix} 0 & \tilde{q} \\ q & 0 \end{pmatrix}, \quad U_{\varepsilon=\pi}(k, \frac{T}{2}) = \begin{pmatrix} q & 0 \\ 0 & \tilde{q} \end{pmatrix}. \quad (42)$$
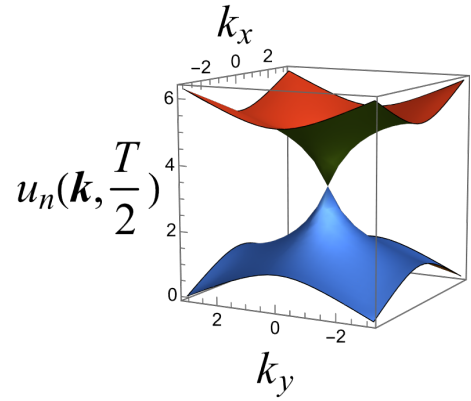
For instance, Eq. (41) gives

$$U_{\varepsilon=\pi}(k, \frac{T}{2}) = \tilde{U}(k) = -\begin{pmatrix} e^{ik\sigma_3} & 0 \\ 0 & e^{-ik\sigma_1} \end{pmatrix} \Rightarrow q = -e^{ik\sigma_1}. \quad (43)$$
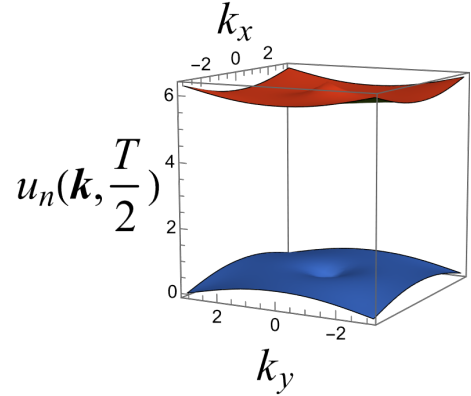
Further, the mirror symmetry M_{xy} in Eq. (36) has eigen-basis

$$|m_{xy}^{(+)}(\alpha, \beta)\rangle = \begin{pmatrix} \alpha \\ 0 \\ \beta/\sqrt{2} \\ \beta/\sqrt{2} \end{pmatrix}, \quad |m_{xy}^{(-)}(\alpha, \beta)\rangle = \begin{pmatrix} 0 \\ \alpha \\ \beta/\sqrt{2} \\ -\beta/\sqrt{2} \end{pmatrix}, \quad (44)$$
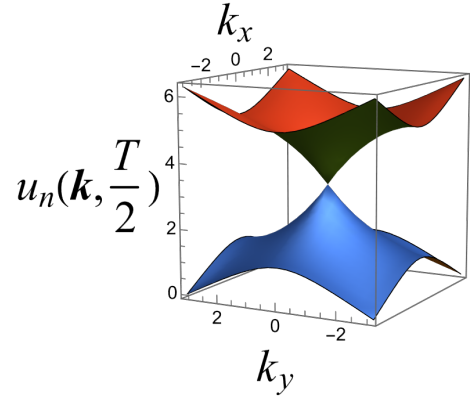
for eigenvalues ± 1 respectively. Here α (or β) is for the projection into chiral symmetry sector $s = +1$ (or $s = -1$), and

(a) Parameter ● in Fig. 6 (c) with $g = 0.25$ in Fig. 6 (a)

(b) Parameter ▲ in Fig. 6 (c) with $g = 1.5$ in Fig. 6 (a)

(c) Parameter ■ in Fig. 6 (c) with $g = 3.5$ in Fig. 6 (a)

FIG. 7. Representative instant spectrum for three points in Fig. 6(c). Each band is doubly degenerate.

$|\alpha|^2 + |\beta|^2 = 1$. Consider the chiral sector $+1$ corresponding to q in Eq. (43), we have the mirror symmetry sector projections as

$$q_{\pm} = \langle m_{xy}^{(\pm)}(1, 0)|\tilde{U}(k)|m_{xy}^{(\pm)}(1, 0)\rangle = -e^{\pm ik}. \quad (45)$$

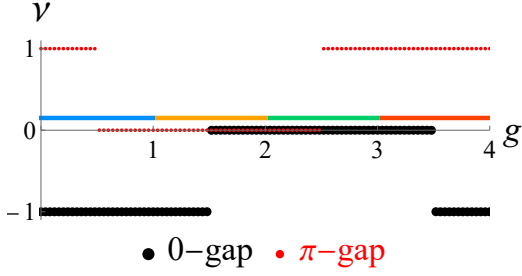Finally, the topological invariant is defined as the mirror-

FIG. 8. The mirror graded winding numbers within the reduced Brillouin zone defined by $M_{xy}(\boldsymbol{k}) = \boldsymbol{k}$.

graded winding number in the IRBZ,

$$
\nu = \frac{\nu_{m_{xy}=+1} - \nu_{m_{xy}=-1}}{2}
$$
$$
= \int_{-\sqrt{2}\pi}^{\sqrt{2}\pi} \frac{dk}{2\sqrt{2}\pi i} \frac{q_+^* \partial_k q_+ - q_-^* \partial_k q_-}{2} = +1. \quad (46)
$$

This predicts the existence of π-mode at the edges of the mirror plane. Similarly, for the 0-gap, one can perform the pro-

jection $q_\pm = \langle m_{xy}^{(\pm)}(0,1)|q|m_{xy}^{(\pm)}(1,0)\rangle$ and compute the invariant. Finally, we present in Fig. 8 a numerical calculation for the mirror-graded winding number, along the parameter contour shown in Fig. 6 (a). Again, we find that such a mirror graded winding number precise prescribes the existence of corner modes in both 0 and π gap, and the results for π-gap coincide with Fig. 6 (b) (c).

V. COMPARISON OF DIFFERENT METHODS

In the previous sections, we discussed two classes of topological invariants. Their major differences are summarized in Table I. We have briefly stressed that the dynamical polarization describes the topology of real-space boundaries, while the dynamical singularity and crystalline-symmetry-graded topological invariants both concern the topology within the reduced Brillouin zone. But in many models, such as that in Fig. 1, these two types of topology may fairly coexist, making their distinctions obscure. Therefore, we would further demonstrate their difference in this section through a modified model on top of that in Fig. 1.

TABLE I. Comparison between different approaches to characterize anomalous Floquet higher-order topology

	Dynamical polarization	Dynamical singularity and crystalline symmetry graded invariant
Topology concerning?	Bulk enforced real space boundary	High symmetry region in Brillouin zone
How to change invariant?	Bulk or edge gap closure	Must be bulk gap closure within symmetric Brillouin zone

Specifically, we would change the Hamiltonian in Fig. 1 (a) into

$$
\gamma h_1 = \gamma(\tau_1 \sigma_0 - \tau_2 \sigma_2) \quad \rightarrow \quad \gamma_x \tau_1 \sigma_0 - \gamma_y \tau_2 \sigma_2 \quad (47)
$$

That is, the hopping strength of h_1 along x and y becomes different. Meanwhile, $\lambda h_{2\boldsymbol{k}}$ in Fig. 1 (b) is kept unchanged. Such a modification still preserves the mirror symmetries along two axes M_x, M_y, but breaks the diagonal mirror symmetry M_{xy}. According to the analysis in Sec. III and IV, the dynamical polarization should still be quantized, while the dynamical singularity are no longer protected. Consequently, this should yield in the following a class of robust corner state protected only by edge topology.

For simplicity, we would focus only on the π-gap for illustrations. Therefore, it will be natural to start from the parameters $(\gamma_x, \gamma_y, \lambda) = (\pi/\sqrt{2})(1, 1, 0.25)$ corresponding to phase ③ in Fig. 2 (a) exhibiting π corner modes only. Then, we start to decrease γ_x, and compare its effects on Floquet spectrum (Fig. 9), dynamical polarization (Fig. 10), and dynamical singularity (Fig. 11).

We first confirm the existence and nature of corner states in Fig. 9. Here, we numerically obtain the Floquet spectrum for the same set of parameters but with different boundary conditions. In Fig. 9 (a) with full periodic boundary condition, we observe that upon decreasing γ_x away from the value of $\gamma_x = \gamma_y$, no bulk gap closure occurs. In contrast, for a stripe geometry with mixed open and periodic boundary conditions in Fig. 9 (b), it is confirmed that an *edge* gap closure shows up around $\gamma_x \approx 1.2$. As such, for a lattice with full open boundary in Fig. 9 (c), the π corner modes vanishes after the edge gap reopens for $\gamma_x < 1.2$, signaling an *edge* topological phase transition.

Next, we apply the two aforementioned methods to the extended model. For the dynamical polarization presented in Fig. 10, we indeed see that the "crossing" at 0.5 occurs right after the edge transition $\gamma_x \geq 1.2$ indicated in Fig. 9 (b), precisely capturing the corner states induced by edge topology. Contrarily, Fig. 11 shows that the dynamical singularity is gapped out immediately when γ_x deviates from the value of γ_y. Such a difference highlights the fact that when M_{xy} is bro-

(a) Torus: Periodic boundary condition along both x, y

(b) Stripe: Periodic boundary condition along y, but open along x

(c) Square: Open boundary condition along both x, y
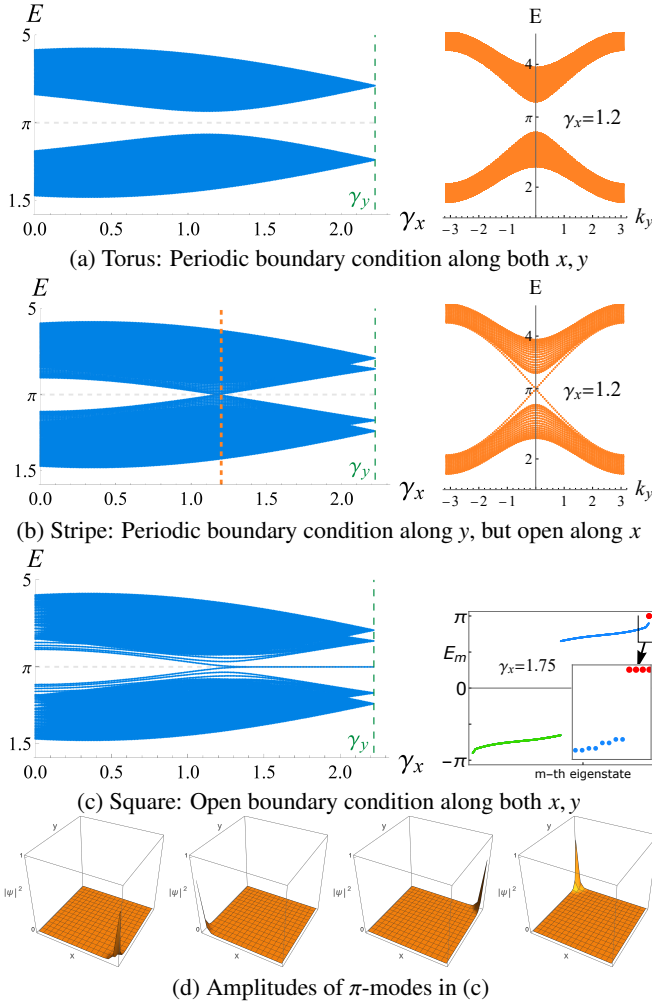

(d) Amplitudes of π-modes in (c)

FIG. 9. Quasienergy spectrum of the Floquet operator under different boundary conditions. Here $(\gamma_y, \lambda) = (\pi/\sqrt{2})(1, 0.25)$ is fixed. Should $\gamma_x = \gamma_y$ (green dashed line), it corresponds to phase ③ in Fig. 2 (a) with π corner modes. Decreasing γ_x below $\gamma_x^{(c)} \approx 1.2$ destroys these corner modes. (a) and (b) clearly show that an edge (rather than bulk) topological phase transition occurs around $\gamma_x^{(c)}$ where the edge π-gap closes while the bulk gap remains open.

ken, only edge topology remains. As a safety check, note that $M_x = \tau_1\sigma_3, M_y = \tau_1\sigma_1$ both *anticommute* with the chiral symmetry $S = \tau_3\sigma_0$, and therefore M_x, M_y, S cannot be simultaneously diagonalized and yield the basis analogous to Eq. (39). That forbids possible protection of dynamical singularity by M_x, M_y too. In connection to the terminology in static higher-order topological insulators, one could dub the system in Fig. 9 – Fig. 11 where only edge topology exists as "boundary obstructed topological phases" [62].

Finally, two caveats are in order.

First, although we use the phrase "edge topology", the physics described by dynamical polarization is not to be confused with that in proximity effects (i.e. embedding an s-wave superconductor onto the surface of a topological insulator [69]). After all, the "edge" layer in Fig. 1 essentially makes no difference from any other bulk layers, unlike the

(a) $\gamma_x = 0.5$ (b) $\gamma_x = 1.0$ (c) $\gamma_x = 1.1$

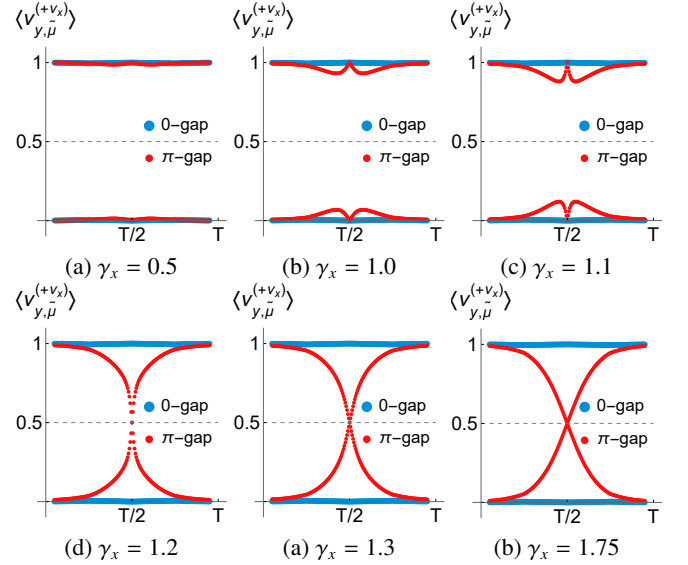(d) $\gamma_x = 1.2$ (a) $\gamma_x = 1.3$ (b) $\gamma_x = 1.75$

FIG. 10. DP for the extended model. We see that the corner states in Fig. 9 (c) is characterized by DP across the edge topological phase transition.
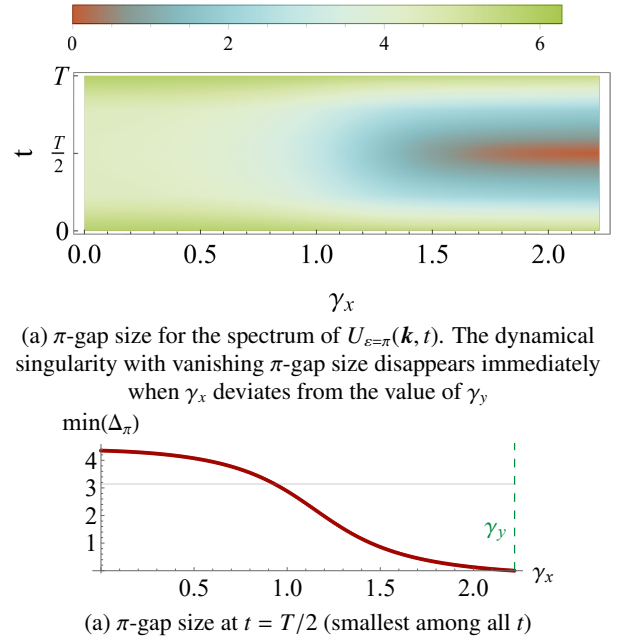

(a) π-gap size for the spectrum of $U_{\varepsilon=\pi}(\boldsymbol{k}, t)$. The dynamical singularity with vanishing π-gap size disappears immediately when γ_x deviates from the value of γ_y

(a) π-gap size at $t = T/2$ (smallest among all t)

FIG. 11. Dynamical singularity for the extended model is immediately gapped out when the M_{xy} is broken by $\gamma_x \neq \gamma_y$, although corner states still exist for certain ranges as shown by Fig. 9 (c).

superconductor which is completely different from the underlying insulator. Instead, edge topology here is enforced by the bulk dynamical quadrupole. Physically, one can see the difference by noting that even if we remove the edge layer (i.e. reduce unit cell number L_y to $L_y - 1$), the "new edge" would still carry nontrivial topology enforced by the bulk dynamical polarization and lead to corner states.

Second, it is helpful to note that the edge topology here differs from the first-order "weak indices" for *each* layer

independently [70]. Following the terminologies for static cases [71], the topology characterized by dynamical polarization is relevant to "extrinsic" AFHOTI, while dynamical singularity and crystalline symmetry graded invariants are related to "intrinsic" AFHOTI. Meanwhile, within the category of extrinsic AFHOTI, in order to observe corner/hinge modes characterized by dynamical polarization, one only needs the open boundaries to satisfy underlying bulk crystalline symmetries [32, 71]. This is because the boundary topology here is enforced by the bulk multiple polarization. In contrast, the weak topological indices will require special open boundaries depending on microscopic model details in order for the boundary modes to exhibit reduced dimensionality [71]. In other words, without fine-tuning of how to cut the boundary, a two-dimensional first order weak insulator will generally demonstrate a usual one-dimensional edge state induced simply by all the weak indices in each layer of the bulk.

VI. OUTLOOK

In this review, we give a pedagogical introduction to several classes of methods to practically obtain the anomalous Floquet higher-order topology, and compare their different physical consequences. Connections to recent developments in static systems are also stressed. Currently, the field of AFHOTI is still at an early stage with rapid development in multiple directions.

One topic that we have not reviewed in detail is the issue of classifications. In addition to those based on dynamical singularity [58, 59], there have also been discussions based on other methods as well. That includes the frequency domain analysis of the edge theory [55] and a K theory classification after mapping evolution operators into enlarged Hamiltonian systems homotopically [2, 60]. In particular, a Floquet system allows for a special class of nonsymmorphic spacetime symmetry, dubbed "spacetime crystals" [55, 60, 72, 73]. These symmetries feature a combined crystalline symmetry operation and temporal translations by a fraction of period T. For instance, the "time glide" (or "time screw") involves a spatial mirror reflection M (or n-fold rotation C_n) combined with time translation by half a period, such as $M_x H(k_x, k_y, t)M_x^{-1} = H(-k_x, k_y, t + T/2)$. Therefore, unique symmetry classes and their associated topological classification could emerge in a strongly driven Floquet system.

Meanwhile, there have been connections between the AFHOTI and several related topics in recent researches. For instance, similar to the case for static symmetry indicator [74, 75], a dynamical symmetry indicator approach has been formulated recently for the Floquet systems [76]. The dynamical symmetry indicator serves as a sufficient (but unnecessary) condition to suggest anomalous Floquet topological systems of both the first and higher orders. The advan-

tage for this method is that it allows for a systematic scanning through various symmetry classes quickly. Also, the issue of obstruction to form global Wannier wave functions, related to the topic of "fragile topology" [77–79], has been generalized into non-interacting first-order anomalous Floquet systems recently [80–82]. It could be of interest to further consider higher-order topological counterparts in the future. Other topics with recent initial explorations include generalizations of AFHOTI to semimetals [83–85], non-Hermitian [86, 87], and interacting systems [88].

Experimentally, the first realization of AFHOTI has been exhibited in acoustic systems [89, 90]. The experiment setting is based on a circuit-like two-dimensional lattice with two sublattices. The detection has resolutions in both real space locations and also in Floquet eigenstate frequency, and therefore essentially results like those in Fig. 2 (b) (c) can be obtained, showing the corner states in both 0 and π gaps.

Meanwhile, it may be desirable for future experiment to also demonstrate the anomalous Floquet higher-order topology directly. A recent cold atom experiment [65, 66] points out a way to detect dynamical singularity by measuring Floquet spectrum gap closure and reopening with the change of certain parameters. That essentially corresponds to the physics in Fig. 6 (b) where with the increase of g, a singularity is gradually "deposited" into $t \in (0, T)$ from $t = T$ as g becomes larger than 2.5. Such a scheme can in principle be directly generalized into higher-order cases. Further, we have shown in Sec. V that for the higher-order cases, the boundary obstructed topological phases escapes the descriptions by dynamical singularity. Thus, it could be a future task to design schemes that could capture the dynamical polarization directly.

Finally, it has been a long-term goal to achieve anomalous Floquet phases in solid state systems, both for the first and higher order cases. The challenge lies at the difficulty to induce driving amplitudes strong enough to be comparable with solid state sample's internal energy scales, which is a typical scenario where anomalous Floquet phases can emerge. Recently, there has been a proposal [91] to exploit phonon interactions to drive a trivial insulator into anomalous Floquet phases protected by nonsymmorphic spacetime symmetries. A realization of the peculiar anomalous Floquet superconductors in solid state systems may offer an alternative way for braiding manipulations in quantum computations by exploiting the simultaneous existence of 0 and π majorana modes [92].

[1] Mark S Rudner, Netanel H Lindner, Erez Berg, and Michael Levin, "Anomalous edge states and the bulk-edge correspondence for periodically driven two-dimensional systems," Phys.

Rev. X **3**, 031005 (2013).

[2] Rahul Roy and Fenner Harper, "Periodic table for floquet topological insulators," Phys. Rev. B **96**, 155118 (2017).

[3] Shunyu Yao, Zhongbo Yan, and Zhong Wang, "Topological invariants of floquet systems: General formulation, special properties, and floquet topological defects," Phys. Rev. B **96**, 195303 (2017).

[4] Andrew C. Potter, Takahiro Morimoto, and Ashvin Vishwanath, "Classification of interacting topological floquet phases in one dimension," Phys. Rev. X **6**, 041001 (2016).

[5] Hoi Chun Po, Lukasz Fidkowski, Takahiro Morimoto, Andrew C. Potter, and Ashvin Vishwanath, "Chiral floquet phases of many-body localized bosons," Phys. Rev. X **6**, 041070 (2016).

[6] Takahiro Morimoto, Hoi Chun Po, and Ashvin Vishwanath, "Floquet topological phases protected by time glide symmetry," Phys. Rev. B **95**, 195155 (2017).

[7] I.-D. Potirniche, A. C. Potter, M. Schleier-Smith, A. Vishwanath, and N. Y. Yao, "Floquet symmetry-protected topological phases in cold-atom systems," Phys. Rev. Lett. **119**, 123601 (2017).

[8] Andrew C. Potter, Ashvin Vishwanath, and Lukasz Fidkowski, "Infinite family of three-dimensional floquet topological paramagnets," Phys. Rev. B **97**, 245106 (2018).

[9] Hoi Chun Po, Lukasz Fidkowski, Ashvin Vishwanath, and Andrew C. Potter, "Radical chiral floquet phases in a periodically driven kitaev model and beyond," Phys. Rev. B **96**, 245116 (2017).

[10] Lukasz Fidkowski, Hoi Chun Po, Andrew C. Potter, and Ashvin Vishwanath, "Interacting invariants for floquet phases of fermions in two dimensions," Phys. Rev. B **99**, 085115 (2019).

[11] Krzysztof Sacha and Jakub Zakrzewski, "Time crystals: a review," Rep. Prog. Phys. **81**, 016401 (2017).

[12] Vedika Khemani, Roderich Moessner, and S. L. Sondhi, "A brief history of time crystals," (2019), arXiv:1910.10745.

[13] Dominic V. Else, Christopher Monroe, Chetan Nayak, and Norman Y. Yao, "Discrete time crystals," Annu. Rev. Condens. Matter Phys. **11**, 467–499 (2020).

[14] Takashi Oka and Sota Kitamura, "Floquet engineering of quantum materials," Annu. Rev. Condens. Matter Phys. **10**, 387–408 (2019).

[15] Gregor Jotzu, Michael Messer, Rémi Desbuquois, Martin Lebrat, Thomas Uehlinger, Daniel Greif, and Tilman Esslinger, "Experimental realization of the topological haldane model with ultracold fermions," Nature **515**, 237–240 (2014).

[16] André Eckardt, "Colloquium: Atomic quantum gases in periodically driven optical lattices," Rev. Mod. Phys. **89**, 011004 (2017).

[17] Monika Aidelsburger, Michael Lohse, C Schweizer, Marcos Atala, Julio T Barreiro, S Nascimbene, NR Cooper, Immanuel Bloch, and Nathan Goldman, "Measuring the chern number of hofstadter bands with ultracold bosonic atoms," Nat. Phys. **11**, 162 (2015).

[18] D. J. Thouless, "Quantization of particle transport," Phys. Rev. B **27**, 6083–6087 (1983).

[19] M. Lohse, C. Schweizer, O. Zilberberg, M. Aidelsburger, and I. Bloch, "A thouless quantum pump with ultracold bosonic atoms in an optical superlattice," Nat. Phys. **12**, 350–354 (2015).

[20] Shuta Nakajima, Takafumi Tomita, Shintaro Taie, Tomohiro Ichinose, Hideki Ozawa, Lei Wang, Matthias Troyer, and Yoshiro Takahashi, "Topological thouless pumping of ultracold fermions," Nat. Phys. **12**, 296–300 (2016).

[21] Takuya Kitagawa, Erez Berg, Mark Rudner, and Eugene Demler, "Topological characterization of periodically driven quantum systems," Phys. Rev. B **82**, 235114 (2010).

[22] Wladimir A Benalcazar, B Andrei Bernevig, and Taylor L Hughes, "Quantized electric multipole insulators," Science **357**, 61–66 (2017).

[23] Wladimir A. Benalcazar, B. Andrei Bernevig, and Taylor L. Hughes, "Electric multipole moments, topological multipole moment pumping, and chiral hinge states in crystalline insulators," Phys. Rev. B **96**, 245115 (2017).

[24] Jiho Noh, Wladimir A Benalcazar, Sheng Huang, Matthew J Collins, Kevin P Chen, Taylor L Hughes, and Mikael C Rechtsman, "Topological protection of photonic mid-gap defect modes," Nat. Photonics **12**, 408 (2018).

[25] Marc Serra-Garcia, Valerio Peri, Roman Süsstrunk, Osama R. Bilal, Tom Larsen, Luis Guillermo Villanueva, and Sebastian D. Huber, "Observation of a phononic quadrupole topological insulator," Nature **555**, 342 (2018).

[26] Christopher W. Peterson, Wladimir A. Benalcazar, Taylor L. Hughes, and Gaurav Bahl, "A quantized microwave quadrupole insulator withtopologically protected corner states," Nature **555**, 346 (2018).

[27] Stefan Imhof, Christian Berger, Florian Bayer, Johannes Brehm, Laurens Molenkamp, Tobias Kiessling, Frank Schindler, Ching Hua Lee, Martin Greiter, Titus Neupert, and Ronny Thomale, "Topolectrical circuit realization of topological corner modes," Nat. Phys. **14**, 925 (2018), arXiv:1708.03647v1.

[28] Frank Schindler, Ashley M Cook, Maia G Vergniory, Zhijun Wang, Stuart SP Parkin, B Andrei Bernevig, and Titus Neupert, "Higher-order topological insulators," Sci. Adv. **4**, eaat0346 (2018).

[29] Frank Schindler, Zhijun Wang, Maia G. Vergniory, Ashley M. Cook, Anil Murani, Shamashis Sengupta, Alik Yu. Kasumov, Richard Deblock, Sangjun Jeon, Ilya Drozdov, Hlne Bouchiat, Sophie Guron, Ali Yazdani, B. Andrei Bernevig, and Titus Neupert, "Higher-order topology in bismuth," Nat. Phys. **14**, 918 (2018).

[30] Flore K. Kunst, Guido van Miert, and Emil J. Bergholtz, "Lattice models with exactly solvable topological hinge and corner states," Phys. Rev. B **97**, 241405 (2018).

[31] Zhida Song, Zhong Fang, and Chen Fang, "$(d-2)$-dimensional edge states of rotation symmetry protected topological states," Phys. Rev. Lett. **119**, 246402 (2017).

[32] Josias Langbehn, Yang Peng, Luka Trifunovic, Felix von Oppen, and Piet W. Brouwer, "Reflection symmetric second-order topological insulators and superconductors," Phys. Rev. Lett. **119**, 246401 (2017).

[33] Luka Trifunovic and Piet Brouwer, "Higher-order bulk-boundary correspondence for topological crystalline phases," Phys. Rev. X **9**, 011012 (2019), 1805.02598v1.

[34] Dumitru Calugaru, Vladimir Juricic, and Bitan Roy, "Higher order topological phases: A general principle of construction," Phys. Rev. B **99**, 041301(R) (2019), arXiv:1808.08965v1.

[35] Raquel Queiroz and Ady Stern, "Splitting the hinge mode of higher-order topological insulators," Phys. Rev. Lett. **123**, 036802 (2019), 1807.04141v2.

[36] Motohiko Ezawa, "Topological switch between second-order topological insulators and topological crystalline insulators," Phys. Rev. Lett. **121**, 116801 (2018), 1806.03007v1.

[37] Fan Zhang, Charles L Kane, and Eugene J Mele, "Surface state magnetization and chiral edge states on topological insulators," Phys. Rev. Lett. **110**, 046404 (2013).

[38] B Seradjeh, C Weeks, and M Franz, "Fractionalization in a

square-lattice model with time-reversal symmetry," Phys. Rev. B **77**, 033104 (2008).

[39] Mao Lin and Taylor L. Hughes, "Topological quadrupolar semimetals," Phys. Rev. B **98**, 241103 (2018), 1708.08457v1.

[40] Motohiko Ezawa, "Higher-order topological insulators and semimetalson the breathing kagome and pyrochlore lattices," Phys. Rev. Lett. **120**, 026801 (2018).

[41] Motohiko Ezawa, "Magnetic second-order topological insulators and semimetals," Phys. Rev. B **97**, 155305 (2018).

[42] Hassan Shapourian, Yuxuan Wang, and Shinsei Ryu, "Topological crystalline superconductivity and second-order topological superconductivity in nodal-loop materials," Phys. Rev. B **97**, 094508 (2018).

[43] Yuxuan Wang, Mao Lin, and Taylor L. Hughes, "Weak-pairing higher order topological superconductors," Phys. Rev. B **98**, 165144 (2018), 1804.01531v2.

[44] Eslam Khalaf, "Higher-order topological insulators and superconductors protected by inversion symmetry," Phys. Rev. B **97**, 205136 (2018).

[45] Xiaoyu Zhu, "Tunable majorana corner states in a two-dimensional second-order topological superconductor induced by magnetic fields," Phys. Rev. B **97**, 205134 (2018).

[46] Zhongbo Yan, Fei Song, and Zhong Wang, "Majorana corner modes in a high-temperature platform," Phys. Rev. Lett. **121**, 096803 (2018).

[47] Qiyue Wang, Cheng-Cheng Liu, Yuan-Ming Lu, and Fan Zhang, "High-temperature majorana corner states," Phys. Rev. Lett. **121**, 186801 (2018), 1804.04711v1.

[48] Tao Liu, James Jun He, and Franco Nori, "Majorana corner states in a two-dimensional magnetic topological insulator on a high-temperature superconductor," Phys. Rev. B **98**, 245413 (2018), 1806.07002v1.

[49] Vatsal Dwivedi, Ciarn Hickey, Tim Eschmann, and Simon Trebst, "Majorana corner modes in a second-order kitaev spin liquid," Phys. Rev. B **98**, 054432 (2018), 1803.08922v1.

[50] Yizhi You, Trithep Devakul, F. J. Burnell, and Titus Neupert, "Higher order symmetry-protected topological states for interacting bosons and fermions," 1807.09788v2.

[51] Alex Rasmussen and Yuan-Ming Lu, "Classification and construction of higher-order symmetry protected topological phases of interacting bosons," Phys. Rev. B **101**, 085137 (2019), 1809.07325v1.

[52] Biao Huang and W. Vincent Liu, "Floquet higher-order topological insulators with anomalous dynamical polarization," Phys. Rev. Lett. **124**, 216601 (2020).

[53] Raditya Weda Bomantara, Longwen Zhou, Jiaxin Pan, and Jiangbin Gong, "Coupled-wire construction of static and floquet second-order topological insulators," Phys. Rev. B **99**, 045441 (2019), 1811.02325v1.

[54] Martin Rodriguez-Vega, Abhishek Kumar, and Babak Seradjeh, "Higher-order floquet topological phases with corner and bulk bound states," Phys. Rev. B **100**, 085138 (2019), 1811.04808v1.

[55] Yang Peng and Gil Refael, "Floquet second-order topological insulators from nonsymmorphic space-time symmetries," Phys. Rev. Lett. **123**, 016806 (2019).

[56] Arnob Kumar Ghosh, Tanay Nag, and Arijit Saha, "Dynamical construction of quadrupolar and octupolar topological superconductors," Phys. Rev. B **105**, 155406 (2022).

[57] Haiping Hu, Biao Huang, Erhai Zhao, and W. Vincent Liu, "Dynamical singularities of floquet higher-order topological insulators," Phys. Rev. Lett. **124**, 057001 (2020).

[58] Rui-Xing Zhang and Zhi-Cheng Yang, "Theory of anomalous floquet higher-order topology: Classification, characterization, and bulk-boundary correspondence," (2020), arXiv:2010.07945.

[59] DinhDuy Vu, Rui-Xing Zhang, Zhi-Cheng Yang, and S. Das Sarma, "Superconductors with anomalous floquet higher-order topology," Phys. Rev. B **104**, l140502 (2021).

[60] Yang Peng, "Floquet higher-order topological insulators and superconductors with space-time symmetries," Phys. Rev. Research **2**, 013124 (2020).

[61] Ching-Kai Chiu, Hong Yao, and Shinsei Ryu, "Classification of topological insulators and superconductors in the presence of reflection symmetry," Phys. Rev. B **88**, 075142 (2013).

[62] Eslam Khalaf, Wladimir A. Benalcazar, Taylor L. Hughes, and Raquel Queiroz, "Boundary-obstructed topological phases," Phys. Rev. Research **3**, 013239 (2021).

[63] Raffaele Resta, "Quantum-mechanical position operator in extended systems," Phys. Rev. Lett. **80**, 1800–1803 (1998).

[64] Di Xiao, Ming-Che Chang, and Qian Niu, "Berry phase effects on electronic properties," Rev. Mod. Phys. **82**, 1959–2007 (2010).

[65] Karen Wintersperger, Christoph Braun, F. Nur nal, André Eckardt, Marco Di Liberto, Nathan Goldman, Immanuel Bloch, and Monika Aidelsburger, "Realization of an anomalous floquet topological system with ultracold atoms," Nat. Phys. **16**, 1058–1063 (2020).

[66] F. Nur nal, Babak Seradjeh, and André Eckardt, "How to directly measure floquet topological invariants in optical lattices," Phys. Rev. Lett. **122**, 253601 (2019).

[67] Martin Rodriguez-Vega, Abhishek Kumar, and Babak Seradjeh, "Higher-order floquet topological phases with corner and bulk bound states," Phys. Rev. B **100**, 085138 (2019).

[68] Raditya Weda Bomantara, Longwen Zhou, Jiaxin Pan, and Jiangbin Gong, "Coupled-wire construction of static and floquet second-order topological insulators," Phys. Rev. B **99**, 045441 (2019).

[69] Liang Fu and C. L. Kane, "Superconducting proximity effect and majorana fermions at the surface of a topological insulator," Phys. Rev. Lett. **100**, 096407 (2008).

[70] M Zahid Hasan and Charles L Kane, "Colloquium: topological insulators," Rev. Mod. Phys. **82**, 3045 (2010).

[71] Max Geier, Luka Trifunovic, Max Hoskam, and Piet W. Brouwer, "Second-order topological insulators and superconductors with an order-two crystalline symmetry," Phys. Rev. B **97**, 205135 (2018).

[72] Shenglong Xu and Congjun Wu, "Space-time crystal and space-time group," Phys. Rev. Lett. **120**, 096401 (2018).

[73] Yang Peng, "Topological space-time crystal," Phys. Rev. Lett. **128**, 186802 (2022).

[74] Hoi Chun Po, Ashvin Vishwanath, and Haruki Watanabe, "Erratum: Symmetry-based indicators of band topology in the 230 space groups," Nat Commun **8**, 50 (2017).

[75] Eslam Khalaf, Hoi Chun Po, Ashvin Vishwanath, and Haruki Watanabe, "Symmetry indicators and anomalous surface states of topological crystalline insulators," Phys. Rev. X **8**, 031070 (2018).

[76] Jiabin Yu, Rui-Xing Zhang, and Zhi-Da Song, "Dynamical symmetry indicators for floquet crystals," Nat Commun **12**, 5985 (2021).

[77] Hoi Chun Po, Haruki Watanabe, and Ashvin Vishwanath, "Fragile topology and wannier obstructions," Phys. Rev. Lett. **121**, 126402 (2018).

[78] Dominic V. Else, Hoi Chun Po, and Haruki Watanabe, "Fragile topological phases in interacting systems," Phys. Rev. B **99**, 125122 (2019).

[79] Seishiro Ono, Youichi Yanase, and Haruki Watanabe, "Sym-

metry indicators for topological superconductors," Phys. Rev. Research **1**, 013012 (2019).

[80] Masaya Nakagawa, Robert-Jan Slager, Sho Higashikawa, and Takashi Oka, "Wannier representation of floquet topological states," Phys. Rev. B **101**, 075108 (2020).

[81] Jiabin Yu, Yang Ge, and Sankar Das Sarma, "Dynamical fragile topology in floquet crystals," Phys. Rev. B **104**, l180303 (2021).

[82] Rui-Xing Zhang and Zhi-Cheng Yang, "Tunable fragile topology in floquet systems," Phys. Rev. B **103**, l121115 (2021).

[83] Yufei Zhu, Tao Qin, Xinxin Yang, Gao Xianlong, and Zhaoxin Liang, "Floquet and anomalous floquet weyl semimetals," Phys. Rev. Research **2**, 033045 (2020).

[84] Weiwei Zhu, Muhammad Umer, and Jiangbin Gong, "Floquet higher-order weyl and nexus semimetals," Phys. Rev. Research **3**, l032026 (2021).

[85] Runnan Zhang, Ken-ichi Hino, and Nobuya Maeshima, "Floquet-weyl semimetals generated by an optically resonant interband-transition," (2022), arXiv:2201.01578.

[86] Hong Wu, Bao-Qin Wang, and Jun-Hong An, "Floquet second-order topological insulators in non-hermitian systems," Phys. Rev. B **103**, l041115 (2021).

[87] Arnob Kumar Ghosh and Tanay Nag, "Non-hermitian higher-order topological superconductors in two-dimension: statics and dynamics," (2022), arXiv:2205.09915.

[88] Kelvin Koor, Raditya Weda Bomantara, and Leong Chuan Kwek, "Symmetry protected topological corner modes in a periodically driven interacting spin lattice," (2022), arXiv:2206.06660.

[89] Weiwei Zhu, Haoran Xue, Jiangbin Gong, Yidong Chong, and Baile Zhang, "Time-periodic corner states from floquet higher-order topology," Nat Commun **13**, 11 (2022).

[90] Weiwei Zhu, Y. D. Chong, and Jiangbin Gong, "Floquet higher-order topological insulator in a periodically driven bipartite lattice," Phys. Rev. B **103**, l041402 (2021).

[91] Swati Chaudhary, Arbel Haim, Yang Peng, and Gil Refael, "Phonon-induced floquet topological phases protected by space-time symmetries," Phys. Rev. Research **2**, 043431 (2020).

[92] Bela Bauer, T. Pereg-Barnea, Torsten Karzig, Maria-Theresa Rieder, Gil Refael, Erez Berg, and Yuval Oreg, "Topologically protected braiding in a single wire using floquet majorana modes," Phys. Rev. B **100**, 041102 (2019).